Digital Image-based Elasto-Tomography: Proof of concept studies for surface based mechanical property reconstruction

Ashton Peters[1], Arnaud Milsant[1], Jérôme Rouzé[1], Lawrence Ray[2], J. Geoffrey Chase[1], Elijah E.W. Van Houten[1]

Keywords: Computational Mechanics, Elasticity, Finite Element Method, Inverse Problem.

[1]Department of Mechanical Engineering, University of Canterbury, Private Bag 4800, Christchurch, New Zealand, ape20@student.canterbury.ac.nz

[2]Eastman Kodak Company, Kodak Research Laboratories, Rochester, New York, USA

ABSTRACT

Digital Image-based Elasto-Tomography (DIET) is a novel method of determining the distribution of elastic properties within the breast. Using an array of calibrated digital cameras and an inverse reconstruction algorithm, DIET allows reconstruction of the internal elastic stiffness distribution of the breast using only motions at the breast surface. This reconstructed stiffness should clearly show carcinoma based on their high elastic property contrast with healthy tissue. Proof of concept studies are presented for both the calibration of the digital imaging system and the inverse reconstruction algorithm. The reconstruction algorithm identified high stiffness tumors in the majority of test cases, even with the addition of random noise based on expected calibration accuracy.

INTRODUCTION

Breast cancer was the most common cancer recorded in New Zealand women in 1999, and significantly was also the most common cause of female cancer death in the same year [1]. Early detection of breast cancer is key to reducing mortality rates, with tumor diagnosis at the local stage increasing the five-year survival rate to over 95% [2].

Mammography is currently the most commonly used and most effective form of breast cancer screening, and its widespread use since the 1970s has significantly increased breast cancer survival rates [3]. However, the majority of women who have had a mammogram experienced some degree of pain or discomfort [4, 5]. Although individuals' description of this pain intensity varies, apprehension of the process in general can lead to ineffective screening frequency in women who are most at risk of breast cancer. Interpreting the results of a mammogram is also a difficult process that requires a skilled radiologist [6]. Mammographic positioning is of crucial importance, with the skill of the film interpreter irrelevant if the scan failed to image the breast correctly. Contrast-enhanced Magnetic Resonance Imaging (MRI) has proved very useful for breast cancer scanning and further medical diagnosis [7]. However, this technique has limited potential for a widespread screening application because of the high cost and the size of the equipment required. Conventional handheld ultrasound scanning is commonly used in analysis of suspected breast lesions. However, the image contrast achieved using conventional ultrasound is low, meaning interpreting the resulting images is

difficult. In addition, the handheld nature of ultrasonic scanning raises issues of geometric repeatability, which is important when considering methods for widespread, repeatable breast screening.

Elastographic techniques for breast cancer screening concentrate on the high elastic property contrast between carcinoma and breast tissue. Separate studies completed by Krouskop et al. [8] and Samani et al. [9] measuring the elastic moduli of human tissue have shown invasive ductal carcinoma to be approximately an order of magnitude stiffer than fibroglandular tissue from a healthy breast. Several novel methods in the field of soft tissue elasticity imaging are currently under development. Magnetic Resonance Elastography (MRE) uses harmonic mechanical displacements measured in a Magnetic Resonance Imaging (MRI) unit to calculate mechanical properties [10, 11, 12]. Ultrasound elastography computes reconstructed mechanical properties based on the propagation of acoustic waves in the breast tissue [13]. Both techniques have had success in identifying high stiffness inclusions, but are yet to undergo extensive screening trials.

Digital Image-based Elasto-Tomography (DIET) is a proposed new imaging technique being developed to take advantage of the high elastic stiffness contrast between carcinoma and breast tissue. This approach utilizes relatively inexpensive digital imaging sensors and computational algorithms to convert motion at the surface of the breast into a description of the elastic properties within the three-dimensional breast volume. A brief description of the main system processes is given below:

1. A steady-state sinusoidal motion is induced in the breast tissue by an actuator at the surface of the breast.

2. Spatially calibrated digital imaging sensors arrayed over the breast capture a sequence of two-dimensional images of reference points on the surface of the breast.

3. An image processing algorithm converts consecutive two-dimensional image data into a three-dimensional motion vector for each reference point on the breast surface.

4. The amplitude of each reference point's motion is used in an inverse reconstruction algorithm that generates an elastic modulus distribution within the three-dimensional breast volume.

The DIET process offers several potential advantages over current breast cancer screening methods. The silicon based technology will be inexpensive to implement, relatively comfortable for the subject, free of ionizing radiation and geometrically repeatable. The result of the process will be an easily interpretable three-dimensional map of tissue stiffness that should clearly show high contrast carcinoma.

This paper describes the digital imaging calibration process required prior to image acquisition, and the initial proof of concept results from the inverse solution algorithm applied to simulated surface motion data. The aim of the two studies performed is to prove the overall concept prior to hardware implementation.

METHODS

There are two main processes involved in the proof of concept study: Camera calibration and motion sensing, and elastic property reconstruction.

Camera Calibration and Motion Sensing

The location of a reference point in the two-dimensional image space of a specific camera is represented by pixel coordinates u and v. This information can be transformed into a three-dimensional camera space position by

$$X_c = u\frac{s}{f}, \quad Y_c = v\frac{s}{f}, \quad \text{and} \quad Z_c = s, \tag{1}$$

where X_c, Y_c, and Z_c are camera space coordinates, f is the focal length of the camera, and s is an unknown parameter. The location of the reference point in world space w can then be calculated using

$$\begin{Bmatrix} X_w \\ Y_w \\ Z_w \end{Bmatrix} = \begin{Bmatrix} X_f \\ Y_f \\ Z_f \end{Bmatrix} + \begin{bmatrix} \quad G_{ij} \quad \end{bmatrix} \begin{Bmatrix} X_c \\ Y_c \\ Z_c \end{Bmatrix}, \tag{2}$$

where X_f, Y_f and Z_f represent the physical location of the camera in world space, and G_{ij} is a rotation matrix specific to each camera. The presence of the unknown s in Equation (1) requires that at least two cameras are used to determine the location of any one reference point in world space, as expected.

Camera calibration involves the comparison of the image space coordinate for a reference point with its known physical position. By rearranging terms in Equation (2), the position of a physical reference point in camera space can be determined using

$$\begin{Bmatrix} X_c \\ Y_c \\ Z_c \end{Bmatrix} = \begin{Bmatrix} X_t \\ Y_t \\ Z_t \end{Bmatrix} + \begin{bmatrix} \quad R_{ij} \quad \end{bmatrix} \begin{Bmatrix} X_w \\ Y_w \\ Z_w \end{Bmatrix}, \tag{3}$$

where X_t, Y_t and Z_t are the location of the world space origin in camera coordinates, and R_{ij} is another rotation matrix specific to the particular camera.

The location of the reference point in image space pixel coordinates is then found using a combination of Equations (1) & (3),

$$\begin{Bmatrix} u.s \\ v.s \\ s \end{Bmatrix} = \begin{bmatrix} \quad M_{ij} \quad \end{bmatrix} \begin{Bmatrix} X_w \\ Y_w \\ Z_w \\ s \end{Bmatrix}, \tag{4}$$

where M_{ij} is a 3×4 calibration matrix. Each calibration point will provide two equations, for u and v pixel coordinates, given its coordinates in world space X_w, Y_w and Z_w. To reconstruct the 12 unknown terms of the calibration matrix, M_{ij}, a minimum of 6 independent calibration points are required to provide the requisite number of equations to solve the system. Additional

calibration points can be used in conjunction with least squares inversion techniques to provide optimal solutions for the calibration problem.

These methods represent standard procedures for 3D photogrammetry and computer vision techniques. For more detailed consideration of these problems the reader is referred to any one of many excellent texts, such as Klette [14], Trucco [15], and Horaud [16].

Elastic Parameter Reconstruction

Model based elastic property reconstruction requires a meaningful mathematical model that relates the response of an object to the excitation applied. In soft tissue elastography, the standard three dimensional, isotropic equations of linear elasticity can be written in Partial Differential Equation (PDE) form as

$$\nabla \cdot \mu \nabla \mathbf{u} + \nabla(\lambda + \mu) \nabla \cdot \mathbf{u} = \rho \frac{\partial^2 \mathbf{u}}{\partial \mathbf{t}^2}, \tag{5}$$

where $\mathbf{u}$ is a vector of the displacements within the domain, μ and λ are material stiffness descriptors also known as Lamé's constants, and ρ is the density of the material. Material stiffness is often also described using Young's Modulus of Elasticity, E, and Poisson's ratio, ν. The relationship between Lamé's constants and these two properties is defined:

$$E = \frac{\mu(3\lambda + 2\mu)}{\lambda + \mu} \quad \text{and} \quad \nu = \frac{\lambda}{2(\lambda + \mu)} \tag{6}$$

Equation (5) cannot be solved analytically for complex geometries and material property distributions, necessitating an approximate solution technique such as Finite Element Methods (FEM). In this case, for an approximate displacement $\hat{\mathbf{u}}$, the problem is formulated as a matrix equation,

$$[A(\mu, \lambda, \rho)]\{\hat{\mathbf{u}}\} = \{\mathbf{b}\}, \tag{7}$$

where $\mathbf{b}$ is the vector of forcing terms, and each element A_{ij} of the matrix $[A]$ is the 3×3 stiffness matrix for the three-dimensional case.

Nonlinear elastic property reconstruction involves the minimization of the squared error between a set of measured displacements, y, and the calculated displacements $f(\theta)$ based on the current parameter estimate, θ. The squared error minimization term takes the form:

$$F = \|y - f(\theta)\|^2, \tag{8}$$

where θ in this case represents the material parameters λ, μ and ρ. Setting $\frac{\partial F}{\partial \theta} = 0$ generates a non-linear system of equations,

$$\frac{\partial F}{\partial \theta} = -2\left(\frac{\partial f}{\partial \theta}\right)^T (y - f(\theta)) = 0. \tag{9}$$

Equation (9) can be solved iteratively using the Gauss-Newton method. For this case, the formulation is written:

$$\theta_{r+1} = \theta_r - \delta_r \left(\frac{\partial^2 F}{\partial \theta^2}\right)^{-1} \left(\frac{\partial F}{\partial \theta}\right) \tag{10}$$

for iteration $r+1$, where δ_r is chosen to influence the step size of the algorithm, ensuring the minimum solution is found. Combining Equations (9) & (10) and developing the approximate Hessian matrix, $\left(\frac{\partial f}{\partial \theta}\right)^T \left(\frac{\partial f}{\partial \theta}\right)$, leads to the full iterative formulation for the problem,

$$\theta_{r+1} = \theta_r + \delta_r \left(\left(\frac{\partial f}{\partial \theta}\right)^T \left(\frac{\partial f}{\partial \theta}\right) + \gamma \mathbf{I}\right)^{-1} \left[\left(\frac{\partial f}{\partial \theta}\right)^T (y - f(\theta))\right], \tag{11}$$

where γ is a regularization term added to the matrix diagonal to aid inversion. This regularization term is recalculated each iteration according to the method described by Marquardt [17], and summarized as:

1. Let $\omega > 1$, and $\gamma^{(r-1)}$ be the value of γ from the previous iteration. In this case $\omega = 10$ and $\gamma^{(0)} = 1$. Compute $F(\gamma^{(r-1)})$ and $F(\gamma^{(r-1)}/\omega)$.

2. If $F(\gamma^{(r-1)}/\omega) \leq F^{(r)}$, let $\gamma^{(r)} = \gamma^{(r-1)}/\omega$.

3. If $F(\gamma^{(r-1)}/\omega) > F^{(r)}$, and $F(\gamma^{(r-1)}) \leq F^{(r)}$, let $\gamma^{(r)} = \gamma^{(r-1)}$.

4. If $F(\gamma^{(r-1)}/\omega) > F^{(r)}$ and $F(\gamma^{(r-1)}) > F^{(r)}$, increase γ by successive multiplication by w until for some smallest n, $F(\gamma^{(r-1)}\omega^n) \leq F^{(r)}$. Let $\gamma^{(r)} = \gamma^{(r-1)}\omega^n$.

RESULTS

Camera Calibration

The calibration process has two major sources of possible error, as both the world space coordinates (X_w, Y_w, and Z_w) and the pixel coordinates (u and v) of each calibration point can contain errors. These errors can be mitigated by the use of multiple calibration points in excess of the six required for a well posed reconstruction of the calibration matrix, M_{ij}. Additionally, the conversion of pixel coordinates for the reference points to world space coordinates will be affected by errors in the pixel coordinates themselves and by errors in the calibration parameters for the camera. These effects can be reduced with the use of additional cameras above the minimum two for the camera to world space conversion problem.

The results in Figures 1–3 detail the effects of the potential errors on the 3D imaging problem. Figures 1 & 2 show the precision of the calibration problem in the presence of errors in both the world space coordinates of the calibration points and their corresponding pixel coordinates. Figure 3 depicts how these calibration errors will affect the general 3D imaging problem of determining the world space coordinates of a reference point from its pixel coordinates.

Figure 1 shows the relationship between the error in calibration parameters and the number of calibration points used on the calibration object when a pixel error of ± 2 is assumed in each camera image. The mean error value

shows little further improvement after approximately 100 calibration points, indicating that 100 calibration points will offer efficient calibration to high precision.

The manufacturing precision of the calibration object also affects the error in calibration parameters, as shown in Figure 2. The mean percentage error begins to plateau at a precision of approximately ± 0.1 mm, where mean calibration parameter errors reach a level of approximately 0.3%. Encouragingly, this manufacturing precision is well within that available with current manufacturing methods.

In the final 3D imaging system errors will be present due to both the inherent pixel error of each camera, and the overall calibration parameter error shown in Figure 2. Figure 3 shows the effect of the overall calibration parameter error and the number of cameras tracking each point on the overall displacement error expected from the system. This figure confirms that errors are sufficiently low for more than 4–5 cameras per reference point, with the total motion error less than 1% of the imaging field so long as the calibration errors are less than 0.3%.

Motion Simulation

The breast model used in all simulations was a quarter-hemisphere 50 mm in diameter. The model was meshed using linear tetrahedral elements, and had a total of 2648 nodes. The domain was split into separate regions to more accurately represent a real breast, each with a different elastic modulus based

on the work of Krouskop et al. [8]. The outermost 20 mm of the volume was assigned a Young's Modulus of 22350 Pa, representing the fatty outer layer of the breast. The remainder of the breast was assigned a Young's Modulus of 35050 Pa, representing the stiffer fibroglandular tissue present in this region. Poisson's ratio was 0.49 and the tissue density was 1020 kg/m^2 throughout the domain.

A total of 27 separate breast models were developed. These models represented a combination of three tumor locations, sizes, and stiffness contrasts to the surrounding tissue. Tumor locations were 15 mm (shallow), 25 mm (middle) and 35 mm (deep) from the breast surface. Diameters were 5, 10 and 15 mm (small, medium and large respectively). Stiffness contrasts were 5x, 10x and 100x the surrounding fibroglandular tissue (Young's Modulus values of 174, 348 and 3480 kPa respectively). These values represent a range of tumor stuffnesses and contrasts below the highest values obtained in relevant clinical testing [8, 9]. Hence, the choices are conservative to test the method.

The motion data required for the reconstruction algorithm used in the experiment was generated through FE simulation, with material properties and boundary conditions as prescribed. Vertical sinusoidal motion was applied over a small semi-circular area at the highest point of the model, as shown in Figure 4. The actuation frequency and amplitude were 100 Hz and 10 mm respectively. The frequency was chosen as it led to mechanical waves in the tissue of wavelength approximately 30 mm, allowing the motion to be

clearly defined on the breast surface. the amplitude of the resulting surface motion is directly proportional to the amplitude of the actuation, therefore 10 mm was chosen arbitrarily and will likely be reduced in a clinical application for patient comfort. Approximate symmetry boundary conditions were implemented at the two internal faces of the model (no in-plane forces or normal displacement), and the bottom face had displacement constrained in all directions as an approximation of the chest wall.

The solution of Equation (7) generated a full vector of steady-state motion amplitudes comprising x, y and z displacements for every node within the model, as seen in Figure 4. To simulate the eventual data collection at reference points on the surface of the breast only, 32 randomly selected nodes on the outer surface were used as simulated clinical data. Measurement error was simulated by the addition of normally distributed noise about the actual surface displacement value with a standard deviation of 5% of the average scale of motion.

Parameter Reconstruction

Because of the reduced number of known surface motions used as inputs to the reconstruction algorithm, the number of reconstructed parameters was also reduced. Full reconstruction would require solving for Young's Modulus at all 2648 nodes, using only x, y and z motion input at 32 points (96 parameters). While this reconstruction would be possible using Singular Value Decomposition (SVD) or a least-squares type method if the input

data was perfect, the addition of noise in this experiment rendered these methods implausible. The parameter space for this surface based inverse problem was reduced by allocating material properties to each node based on which tissue region it occupied, i.e. fatty, fibroglandular or tumor. While impractical in real life applications due to the necessary *apriori* knowledge of internal tissue structure, this method was useful for proving the concept of surface motion-based elasticity reconstruction. In a final clinical application of the DIET system, the number of reconstructed parameters would be many times greater, with each parameter associated with only a small volume of the breast [11]. This approach will allow higher resolution reconstruction of the stiffness within the breast volume without any prior knowledge of the internal structure of the breast, but at greater computational cost than the simple approach used here to prove the concept.

An inverse reconstruction algorithm was developed in Fortran 77, based on a method already in use for MRE data [18]. The inverse reconstruction for all 27 models was completed using a limit of 300 iterations per motion data set, with an initial guess of 24 kPa for the Young's Modulus of all three regions. The Fortran code was compiled and executed on an AMD Athlon XP 1600+ workstation with 1024 Mb RAM, running RedHat Linux 7.3. Each case was run to 300 iterations, or until such a point as the reconstructed tumor stiffness was within 5% of the actual value. Each iteration took approximately 1.5 minutes to complete.

Reconstruction Results

Figure 5 shows the convergence of the reconstruction algorithm for one of the 27 test cases. This example had a 10 mm diameter tumor situated 25 mm below the surface of the breast, with Young's Modulus of 174 kPa. The breast tissue values converge at about iteration 40, though the two stiffness values reached are approximately the inverse of the true material properties. This result is most likely due to the existence of multiple solutions for this symmetric breast model with highly constrained geometry and similar stiffness of the fatty and fibroglandular regions. By iteration 71 the reconstructed tumor value was within 5% of the true stiffness, though the value had not converged fully at this stage. This result was typical of the majority of cases in this study, where the tumor was identified as having high stiffness after the first few iterations, but the exact stiffness value did not converge until later iterations, if at all. Further development of the reconstruction algorithm will help this convergence become more conclusive.

Both the true and reconstructed Young's Modulus distributions for the same case are shown in Figure 6, generated by interpolating nodal stiffness values in three dimensions then sampling through the plane of the figure. The high stiffness of the tumor is clearly identified by the algorithm. Because the three reconstructed parameters were assigned based on the known geometry and physiology of the model, the algorithm was not aiming to reconstruct the location of the tumor or the fatty/fibroglandular tissue interface, but simply the stiffness of these regions.

Figure 7 is a summary of the results obtained for all 27 cases. The success rate of the algorithm is nearly constant across the full range of tumor stiffness contrasts. Of particular significance is the algorithm's identification of a tumor in all the deep, low-contrast cases (A). These are situations where conventional screening and diagnosis modalities have had problems. The reconstruction appeared to struggle with cases where the tumor was large and extremely high contrast (C), even though these would initially appear to be the easiest cases to reconstruct. It is most likely that some of these cases did not succeed due to issues with the numerics of the reconstruction algorithm. The algorithm has been found to be sensitive to the initial parameter stiffness guess, and it appears that in a number of the high stiffness tumor cases that using the same initial guess of 24 kPa is no longer suitable, leading to convergence to an incorrect solution. Further development of the reconstruction algorithm, including the possible development of a seperate initial-guess finding algorithm, will aid in the reconstruction of these cases.

CONCLUSION

The aim of the study was to show that the reconstruction algorithm developed could successfully identify the stiff tumors in simulated breast models. Results from the digital imaging calibration study showed that the motion error expected from the system will be below the 5% noise value added to the motion data for this study. Tumors were identified in 17 out of 27 cases modelled, although the convergence of the algorithm was not conclusive in many

cases. Further modifications to the reconstruction code will allow the solution of nodal stiffness values throughout the entire breast volume, allowing both the position and stiffness of the tumor to be identified.

References

[1] New Zealand Health Information Service. *Cancer: New Registrations and Deaths 1999*. New Zealand Ministry of Health, 2002.

[2] V.C. Cokkinides, A. Samuels, E.M. Ward, and M.J. Thun. *Cancer Prevention & Early Detection Facts & Figures*. American Cancer Society, 2004.

[3] L. Tabar, M. Yen, B. Vitak, H.T. Chen, R.A. Smith, and S.W. Duffy. Mammography service screening and mortality in breast cancer patients: 20-year follow-up before and after introduction of screening. *The Lancet*, 361:1405–1410, 2003.

[4] A. Asghari and M.K. Nicholas. Pain during mammography: the role of coping strategies. *Pain*, 108:170–179, 2004.

[5] R. Sapir, M. Patlas, S.D. Strano, I. Hadas-Halpern, and N.I. Cherny. Does mammography hurt? *Journal of Pain and Symptom Management*, 25:53–63, 2003.

[6] D.B. Kopans. *Breast Imaging*. Lippincott-Ravens, Philadelphia, PA, second edition, 1998.

[7] B. Bone, P. Aspelin, L. Bronge, and B. Veress. Contrast-enhanced MR imaging as a prognostic indicator of breast cancer. *Acta Radiol*, 39:279–284, 1998.

[8] T.A. Krouskop, T.M. Wheeler, F. Kallel, B.S. Garra, and T. Hall. Elastic moduli of breast and prostate tissues under compression. *Ultrasonic Imaging*, 20:260–274, 1998.

[9] A. Samani, J. Bishop, C. Luginbuhl, and D.B. Plewes. Measuring the elastic modulus of ex vivo small tissue samples. *Phys. Med. Biol.*, 48:2183–2198, 2003.

[10] R. Muthupillai, P. J. Rossman, D. J. Lomas, J. F. Greenleaf, S. J. Riederer, and R. L. Ehman. Magnetic resonance elastography by direct visualization of propagating acoustic strain waves. *Science*, 269:1854–1857, 1995.

[11] E.E.W. Van Houten, M.M. Doyley, F.E. Kennedy, J.B. Weaver, and K.D. Paulsen. Initial in vivo experience with steady-state subzone-based MR elastography of the human breast. *Journal of Magnetic Resonance Imaging*, 17:72–85, 2003.

[12] R. Sinkus, J. Lorenzen, D. Schrader, M. Lorenzen, M. Dargatz, and D. Holz. High-resolution tensor MR elastography for breast tumor detection. *Phys. Med. Biol.*, 45:1649–1664, 2000.

[13] M.M. Doyley, P.M. Meaney, and J. Bamber. Evaluation of an iterative reconstruction method for quantitative elastography. *Phys. Med. Biol.*, 45:1521–1540, 2000.

[14] R. Klette, K. Schlüns, and A. Koschan. *Computer Vision, Three-Dimensional Data from Images.* Springer-Verlag, Singapore, 1998.

[15] E. Trucco and A. Verri. *Introductory Techniques for 3D Computer Vision.* Prentice-Hall, New Jersey, USA, 1998.

[16] R. Horaud and O. Monga. *Vision par Ordinateur: Outils Fondamentaux.* Editions Hermès, Paris, 1995.

[17] D.W. Marquardt. An algorithm for least-squares estimation of nonlinear parameters. *SIAM Journal of Applied Mathematics*, 11:431–441, 1963.

[18] E.E.W. Van Houten. *Mechanical Property Reconstruction from MR Detected Harmonic Displacement Data.* PhD thesis, Thayer School of Engineering at Dartmouth College, 2001.

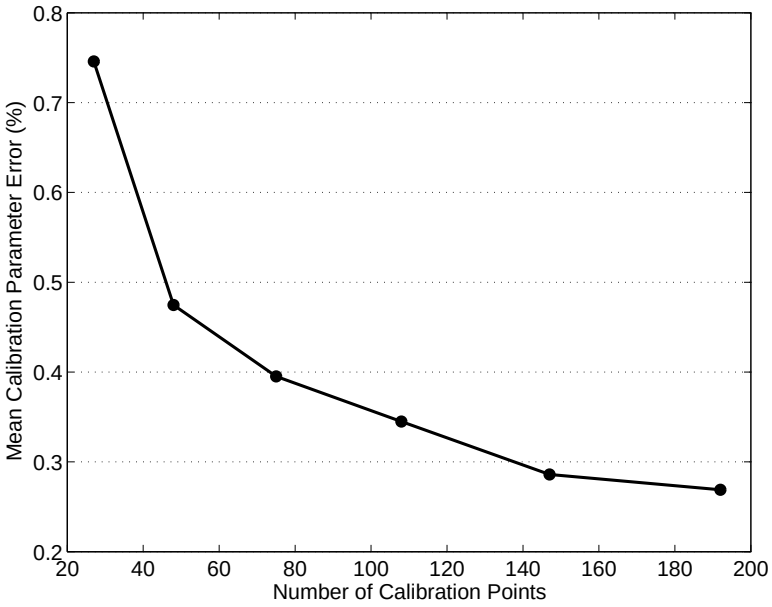

Figure 1: Mean percentage error in calibration parameters as a function of the number of calibration points used, in the presence or an image coordinate error of ± 2 pixels.

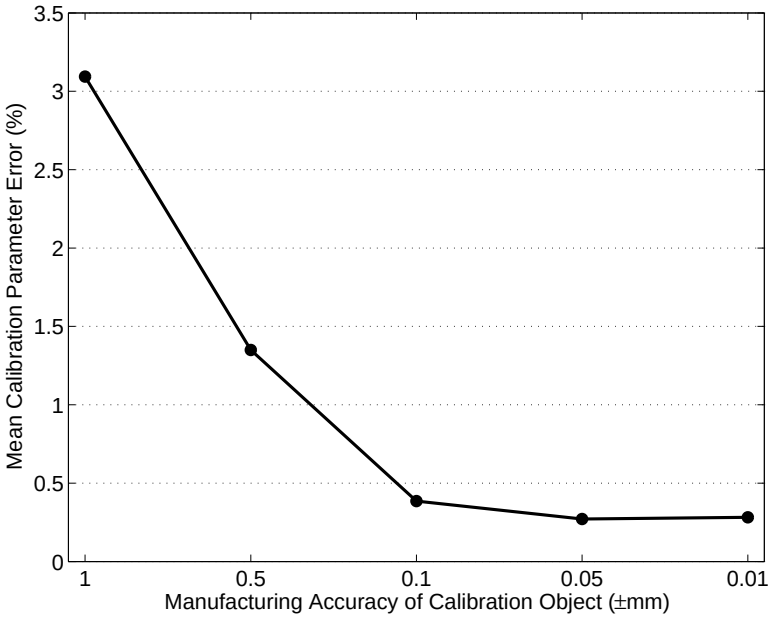

Figure 2: Mean percentage error in calibration parameters as a function of the manufacturing precision of the calibration object. Based on 100 calibration points and an image coordinate error of ± 2 pixels.

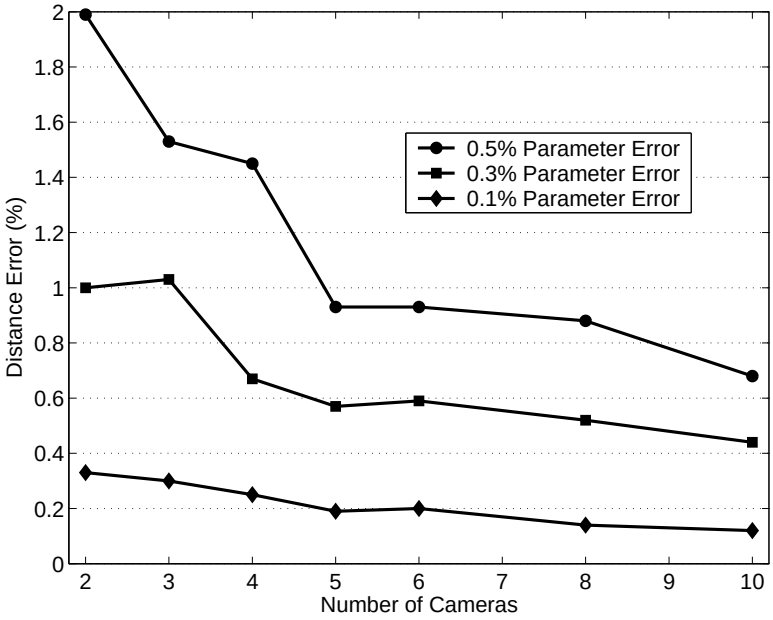

Figure 3: Total distance error as a function of the number of cameras used and the mean percentage error in calibration parameters. Image coordinate error is ± 2 pixels.

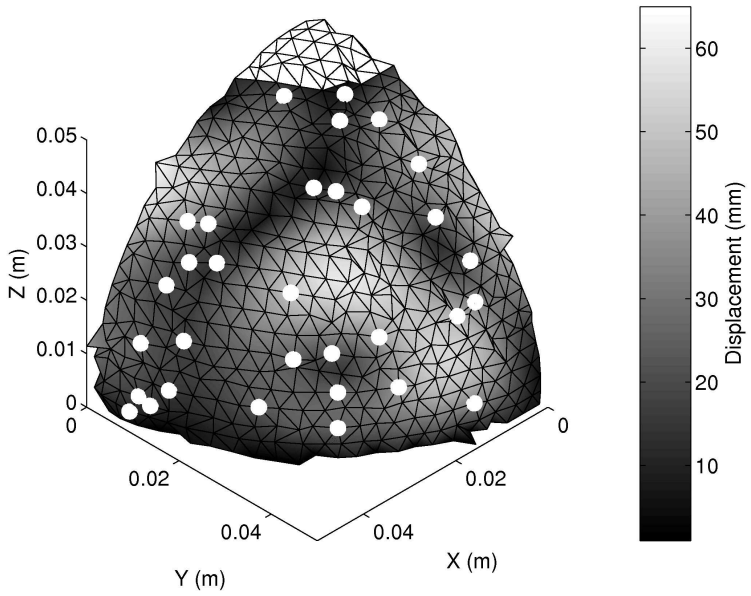

Figure 4: Displacement amplitudes (in mm) generated by forward solution of Equation (7) with a 174 kPa, 10 mm diameter tumour located 25 mm below the surface of the breast. The 32 randomly selected surface nodes used in motion sampling are identified, as is the approximate actuated region (shaded).

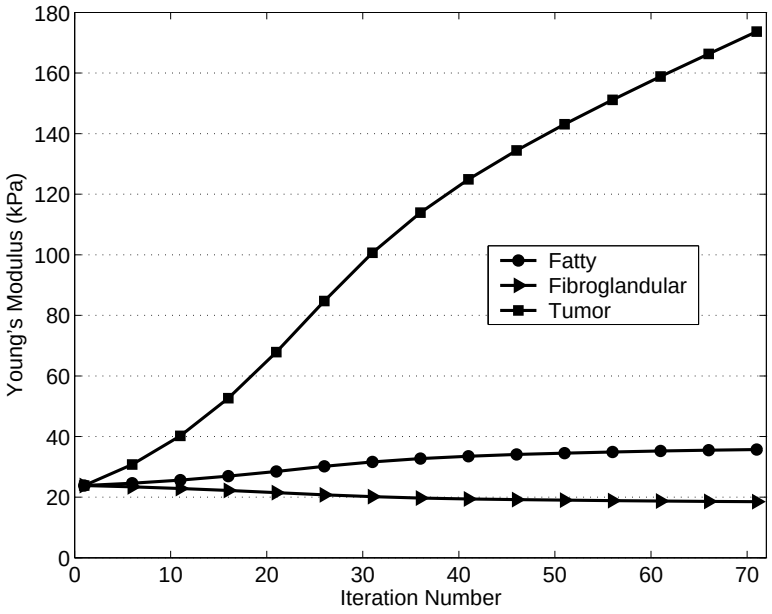

Figure 5: Convergence of the reconstruction algorithm over the first 71 iterations. The actual tumour modulus was 174 kPa, inner modulus 35 kPa, and outer modulus 22 kPa.

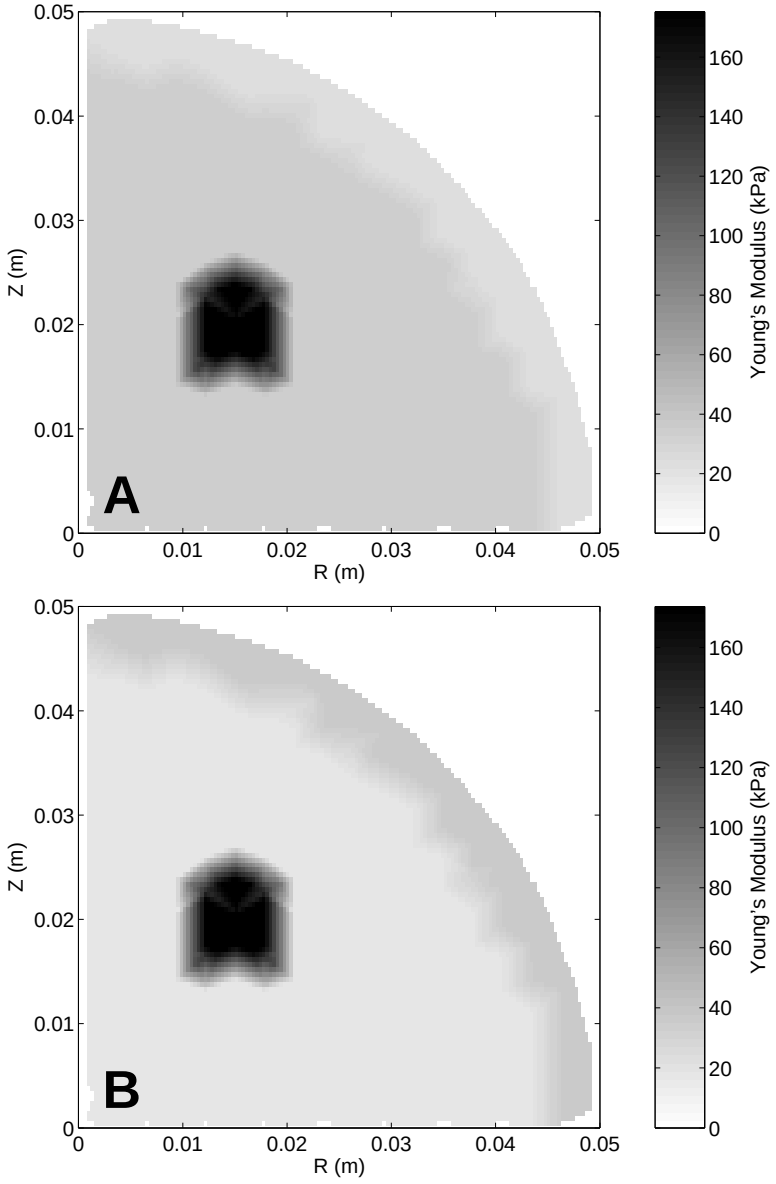

Figure 6: True (A) and reconstructed (B) stiffness values (in kPa) for the same case as Figure 4 after 71 iterations. The plane of both figures passes through the center of the tumour.

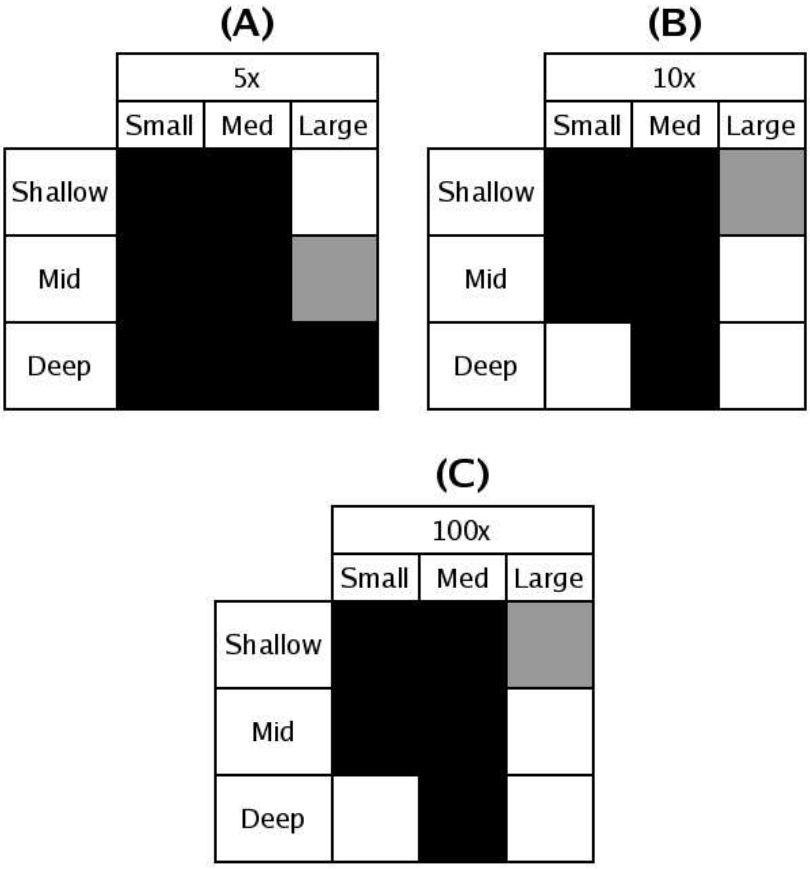

Figure 7: Summary of the reconstruction results from the 27 cases in the study. Black represents the tumor being identified as high stiffness. White is a case where the reconstruction did not identify the tumour as being of higher stiffness, and grey fill represents an inconclusive result.